Field-based prediction of localized anodic dissolution events taking place on ZnAl alloy coatings in the presence of 5% NaCl solution

S. G. R. Brown & N. C. Barnard
School of Engineering, Swansea University, UK

Abstract

An extension to a previously developed numerical model is presented that predicts the sites of localized anodic dissolution on exposed surfaces of ZnAl alloy coating often employed in the protection of steel-strip substrate material. Long-established thermodynamic concepts and galvanic-coupling mechanisms are used to identify sites susceptible to local metallic dissolution. Estimation of metal loss over time is linked to the electrode potentials predicted at the exposed alloy surface. Both alloy composition and the concentration of multiple species in the NaCl solution are considered in determining these electrode potentials. The temporal evolution of the Zn-Al-Fe system – represented using a cellular automaton framework – is predicted via field-based calculations on steady-state voltage and non-steady state diffusion/migration fields. Concentration perturbations in the electrolyte are captured and resultant potential fields are generated using a straight-forward finite difference technique on an irregular-structured computational grid. The influence of the microstructural features in the ZnAl alloy coatings is assessed in terms of metal loss, current density fields and pitted-depth. Simulated results are validated at the meso-scale in comparisons made to experimental observations in accelerated testing of these alloys in concentrated aqueous NaCl solutions. Simulations have been performed that quantitatively assess the localized corrosion at the surface of ZnAl alloy coatings and cut-edge scenarios where Zn, Al and Fe are exposed. The model is extended to predict the effect of altering the processing conditions, i.e. cooling rate and coating thickness.

Keywords: Zn-Al coatings, galvanic corrosion, de-alloying, finite difference.

WIT Transactions on State of the Art in Science and Engineering, Vol 99, © 2017 WIT Press
www.witpress.com, ISSN 1755-8336 (on-line)
doi:10.2495/978-1-78466-249-3/014

1 Introduction

In an effort to protect steel from the deleterious effects of corrosion, it has been a long-standing practice to use zinc and zinc-bearing alloys as coatings. The use of Galfan-type coatings to protect sheet is well-established and forms the substrate for much of the organically coated cladding and guttering of modern buildings. Galfan-type coatings are typically applied via hot-dip routes and the coating thickness, alloy composition and bath chemistry are the focus of much attention [1–3]. A further attempt to model the micro-scale corrosion effects experienced by ZnAl alloy coatings applied to a 0.47 mm thickness mild steel substrate is presented here.

Whilst the performance of the zinc-aluminium coatings themselves is of interest, the performance of these coating when both coating and steel substrate is exposed, i.e. at a cut-edge, is of primary concern since the coating surface is protected by an organic coating layer. During cooling of the coating from the ZnAl hot-dip bath, at ~4.5wt.% Al, primary zinc dendrites solidify within a predominantly lamellar ZnAl (~5wt.% Al) eutectic. During subsequent accelerated aqueous corrosion testing it is the zinc from the dendritic phase that undergoes anodic dissolution via the equation

$$Zn_{(s)} \rightarrow Zn^{2+}_{(aq)} + 2e^{-} \tag{1}$$

In the case of the surface exposure of the metallic coating layer, it is the eutectic phase that acts exclusively as the cathodic surface, whereas in the case of cut-edge exposure, the coupled steel acts cathodically with respect to zinc. In aerated solutions at near-neutral pH, these represent the sites for the supporting oxygen reduction reaction:

$$O_2 + 2H_2O + 4e^{-} \rightarrow 4OH^{-}_{(aq)} \tag{2}$$

During the processes described by eqns (1) and (2), dissolution from the coating layer gives rise to the deposition of a hydroxide layer; impeding the cathodic oxygen reduction reaction [4]. This reaction involves the rapid hydrolysis of water via the equations

$$Zn^{2+} + H_2O \rightarrow ZnOH^{+} + H^{+} \tag{3}$$

$$ZnOH^{+} + H_2O \rightarrow Zn(OH)_2 + H^{+} \tag{4}$$

In order to predict the localized degradation experienced by these steel coatings in the surface and cut-edge situations, eqns (1)–(4) need to be adequately described by a model. Here, the evolution and movement of anions and cations, in addition to the effect of electrical potential on the kinetics of these processes, is included.

The model described here has been developed from a metallurgical standpoint, rather than an electrochemical one and originated as a cellular automata (CA) finite difference model. This approach dealt with the evolution of a representative concentration and electrical potential throughout the electrolyte only [5]. The

model was able to predict morphological features such as localized corrosion pits and capping but was limited to qualitative simulation. However, the CA method has found alternative applications in the growth of corrosion pits where use of CA and Monte Carlo (MC) has been studied [6], including an associated probability for re-passivation and film formation. The CA approach has also been employed in simulating the simple corrosion process taking place at an electrode [7] and most recently in simulating the initiation and growth of multiple pits [8].

Multiple concentration fields are used here in an attempt to capture the dominant effects brought about by eqns (1) and (2) on the spatially discrete anodic and cathodic areas formed during exposure to 5% NaCl solution. Multi-ion electrolyte simulation has also been documented [9] using a nested radial basis function (RBF) approach to predict concentration profiles around a rotating disk. Here, the evolution of $[M^{n+}]$, $[O_2]$, $[OH^-]$ and $[H^+]$ fields around a planar interface is predicted, governed by corrosion rates determined using data obtained from the rotating disc technique.

Previously [3], quantitative predictions regarding the corrosion experienced at the cut-edge with respect to the cooling rate applied to the Galfan-type coating have been shown to be in agreement with experimental findings [1]. However, the trend in corrosion rate at the surface of the ZnAl coating layer was inconclusive. Refinement of the current model has resulted in the observed trend being replicated in simulations and an overview of the results is given here. As an extension to the work, modelling the cut-edge corrosion behaviour has been extended to predict the corrosion rate experienced by steel that has been coated at different weights in slightly differing compositions [3]. The result of these alterations in processing conditions is a change in primary phase fraction (β-Zn) and dendrite morphology.

The experimental work carried out by Elvins *et al.* [1] and Penney *et al.* [3] has been performed using *in situ* corrosion studies based on the scanning vibrating electrode technique (SVET) [10]. The SVET measures the voltage drop over an amplitude of ~30 μm giving a measure of the vertical current density, J_y ($A \cdot m^{-2}$), 100 μm above a corroding surface. An estimation of the material loss experience can then be made from the current density recorded at discrete time intervals.

2 The model

The algorithm used in the model is described in more detail below. There are effectively four main sections to the algorithm:

1. Set up: geometry and initial values on the computational mesh.
2. Determination of electrical potential throughout the solid electrolyte.
3. Dissolution/deposition.
4. Diffusion/migration of multiple species in electrolyte.

2.1 Initialization

The model uses an irregular structured cell-centred finite difference computational mesh. Grid spacings are typically 1–5 μm for cells in the coating layer and rise to

10-25 μm in steel cells close to the centre of the substrate and electrolyte cells far from the solid-liquid interface. The microstructure of the coating layer is entirely synthetic; however, the geometry of the dendritic phase and volume fraction of this primary phase is based upon metallographic observation.

Once a computational mesh has been set up, all variables are initialized and the simulation begins. Each site on the mesh is described by several variables. For electrolyte sites and partially corroded sites these include concentration, C_n, (individual fields for M^{n+}, dissolved O^2, OH^-, and H^+), volume fraction of corrosion product, p, volume fraction of solid material in a cell (to allow cells to corrode gradually), *frac*, and electrical potential, ϕ. Un-corroded solid cells are defined by electrical potential, ϕ, and whether the site is primary Zn, eutectic, inert (polymeric material) or steel substrate. In all cases below, the side faces of the computational mesh possess an insulation boundary condition.

2.2 Electrical potential

The first stage in calculating the electrical potential field, ϕ is to subdivide all elements into 4 groups; electrolyte only elements, electrolyte interface elements, solid interface elements and solid only elements.

Interface elements are any elements where electrolyte and solid materials are in contact, they may be solid elements in contact with electrolyte or vice versa. They will also include all those elements that are partially corroded and contain both solid and electrolyte components (i.e. $0 < frac < 1$). The electrode potential, ϕ_0 (V) at all electrolyte interface elements is calculated (weighted via areas in contact for any given element) using the equation

$$\varphi_0 = E_0 - \frac{RT}{nF}\ln\left(\frac{[Ox]}{[Red]}\right) \tag{5}$$

where E_0 is the standard electrode potential (vs. standard hydrogen electrode) in volts, R the molar gas constant ($J \cdot K^{-1} \cdot mol^{-1}$), n the electronic charge, T the temperature (K) and $[Ox]$ and $[Red]$ are the concentrations of the oxidized and reduced form of the species ($mol \cdot dm^{-3}$); F is Faraday's constant ($C \cdot mol^{-1}$).

These calculated electrolyte interface electrical potentials are then used as Dirichlet boundary conditions to determine the electrical potential field throughout the solid elements (solid interface elements and solid only elements) via the Laplace equation. For solid interface elements (which may be partially electrolyte), the electrical conductivity ($S \cdot m^{-1}$) is calculated via

$$\kappa^* = \left(\kappa_{solid}\right)^{frac}\left(\kappa_{electrolyte}\right)^{1-frac} \tag{6}$$

A precursor step to solving the electrical potentials within the electrolyte is carried out, whereby electro-neutrality is enforced at the solid-electrolyte interface via the adjustment of all solid-containing interface cells. These potentials are held as Dirichlet boundary conditions and the final electrical potential field throughout the electrolyte is calculated using

$$\nabla(\kappa_{electrolyte}\nabla\phi) = 0 \tag{7}$$

2.3 Dissolution/deposition

The amount of dissolution that may occur at interface elements containing solid over the current time increment, Δt (s), is calculated via the equation

$$i = i_0\left[\exp\left(-\frac{\alpha nF\eta}{RT}\right) - \exp\frac{(1-\alpha)nF\eta}{RT}\right] \tag{8}$$

where i_0 is the exchange current density (A·m^{-2}), α is the transfer coefficient and η is the overpotential (V); (ϕ_0-E_0) is predicted using eqn (5); the total dissolution current is defined as $i_{dissolution}$.

Parameters necessary to determine the corrosion rate of these cells are derived from rotating disk experimentation carried out in 5% NaCl. Polarization curves obtained for pure zinc and commercially pure aluminium are shown in Fig. 1. In the case of dissolution of the eutectic phase, two rates are calculated for zinc and aluminium and a harmonic mean is applied to describe the rate of degradation, weighted by volume fractions present in the eutectic phase. However, the amount of corrosion that will occur will depend on the maximum cathodic support that is available, controlled by the diffusion of oxygen to the surface. The availability of oxygen during the current time step, Δt, is determined by the availability of oxygen within one diffusion length (m), of the interface. This total is defined as $i_{capacity}$. If $i_{capacity} < i_{dissolution}$ then the amount of corrosion to occur during the current time increment is scaled down uniformly for each element so that $i_{capacity} = i_{dissolution}$.

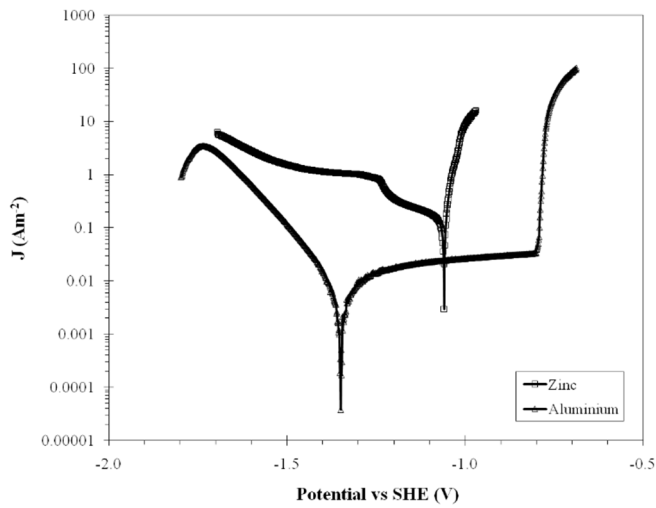

Figure 1: Polarization curves in 0.86M NaCl of a zinc and aluminium electrode.

Each corroding interface site will now have its amount of solid material, *frac*, reduced. Concentration contributions of M^{n+}, O_2 and OH^- from each solid interface cell are distributed geometrically to adjacent electrolyte interface cells.

It is assumed that 5–10% of the volume of material that is lost during dissolution over the time step is re-deposited at the surface of the material as corrosion product. Electrolyte interface sites are selected for corrosion product deposition according to voltage and concentration tolerances and here further ionic concentration contributions arise in M^{n+} and H^+.

2.4 Diffusion

Fickian diffusion (not including interaction terms but including migration effects where appropriate) is carried out for four species within the electrolyte, $[M^{n+}]$, $[O_2]$, $[OH^-]$ and $[H^+]$, according to the standard equation

$$\frac{\partial c_i}{\partial t} = -\nabla\left(D_i \nabla c_i\right) + z_i F \nabla (u_i c_i \nabla \phi) \quad i = 1,4 \tag{9}$$

where D_i is the diffusion coefficient ($m^2 \cdot s^{-1}$) in 0.86M NaCl solution at 298 K, C_i is the molar concentration ($mol \cdot dm^{-3}$) and u is the ionic mobility ($m^2 s^{-1} V^{-1}$) of species i. Side faces of the computational mesh are insulated whereas the top and bottom faces are both fixed at the initial concentration value. For corroding cells at the interface that contain corrosion products, an effective diffusion coefficient, D_{eff}, must be calculated. In the absence of accurate data, this is done using a quadratic form [11] so that the effect of corrosion product at the surface is to increasingly prevent diffusion occurring through that cell. Finally, once the diffusion step is completed for all four species, both [OH-] and [H+] are adjusted to enforce the condition $[OH^-].[H^+] = 10^{-14}$ at all elements containing electrolyte.

3 Results and discussion

During previous investigations, the predicted trend at the cut-edge of Zn – 4.5wt.% Al coating layers that have been cooled at different rates replicated that from SVET experimentation [3]. However, the predicted trend reported in Brown and Barnard [11] did not match that observed. To this end, changes have been made to the solid model that not only better represent the microstructures of the coatings, but also surface depressions around eutectic grain boundaries have been better represented. Again, the cooling rates described here relate to the power output of the coolers that are used after the hot-dip bath and so are expressed as a percentage of the total capability rather than an absolute cooling rate usually associated with microstructural solidification, that is, 55%, 80% and 100%. All cooling rates simulated correspond to 25 μm coating thickness and primary-Zn fraction of 20%.

A further examination of the extended model was performed in the cut-edge situation. This involved simulating the localized effect brought about by galvanic corrosion when the weight of the Galfan-type coating applied is altered. Changes in the coating weight and associated changes in the coating composition modelled are outlined in Table 1.

Table 1: Properties of Galfan-type coatings applied at different weights [3].

Coating Weight (gm^{-2})	Coating thickness (μm)	Al content (%)	β-Zn (%)
150	16.5	4.5	32.6
255	21.5	4.8	22.0
300	39.0	4.9	16.8

3.1 Anodic dissolution

The anodic dissolution modelled using eqns (1) and (8) can be seen to give rise to perturbations in metal cation concentrations from zinc-rich phases present in both surface and cut-edge cases shown in Fig. 2 below. Despite the fact that the eutectic material is permitted to act anodically and cathodically in the case of the cut-edge corrosive case (Fig. 2(a)), perturbations predominantly arise from regions occupied by zinc dendrites owing to the weighting applied in eqn (8) bringing the dissolution rate of the ZnAl eutectic close to that of pure aluminium.

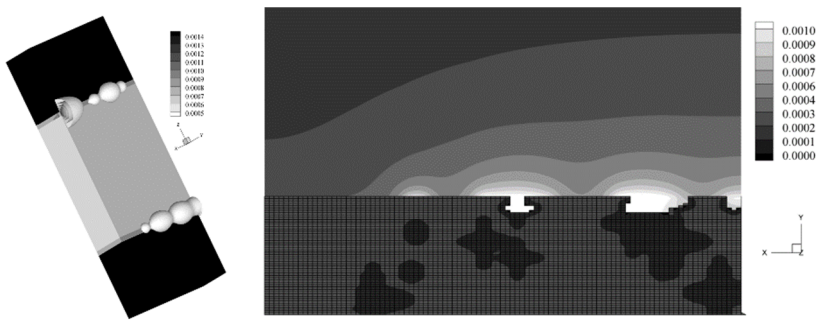

Figure 2: M^{n+} [M] Concentration fields predicted around solid model of 150 gm^{-2} alloy coating after 9.6 hours exposure: (a) Iso-contours with bulk electrolyte removed, and (b) 2D section of ZnAl coating.

The distribution of cation concentration across the cut-edge is in agreement with studies of a Fe/Zn galvanic couple [10]. Diffusional effects are in evidence in Fig. 2(b) where the highest iso-contour of cation concentration can be seen to exist within a pit formed by dissolution from a much smaller dendrite. A reduced zinc loss can be seen to be offset by the more tortuous route from the pit, impeded further still by closer proximity of cells containing corrosion product.

3.2 Cathodic oxygen reduction

The result of the supporting cathodic reaction, eqn (2), on the dissolved oxygen field can be seen for cut-edge case and surface corrosion in Figs. 3(a) and (b), respectively. The lowest values of oxygen can be seen in both to be lowest at sites where entire solid removal has taken place, i.e. the longest diffusion path. This has been distinguished in Fig. 3(b) at A, whereas at B it is the reduction of oxygen that

has been the cause of local decrease in oxygen. It can be seen that the cathodic reaction creates a more diffuse field at the cut-edge owing to the presence of the steel substrate. It is only at these sites that the overpotential, η, in eqn (8) will be affected as cathodic and anodic processes are identified on a metallurgical basis.

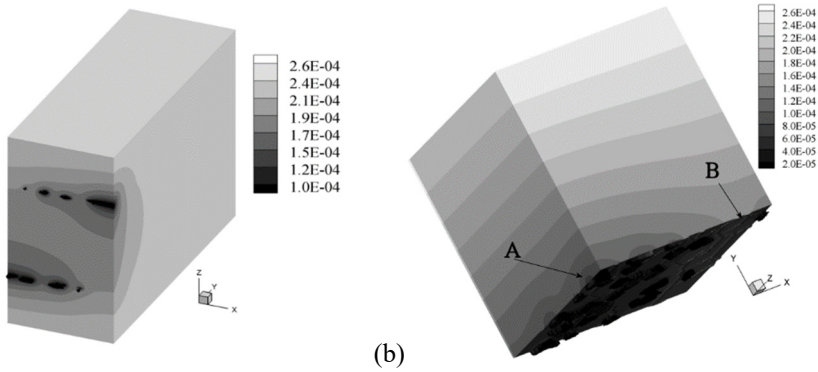

(a) (b)

Figure 3: Dissolved oxygen (mol dm^{-3}) in 5% NaCl solution after (a) 12 hours contact with 255 gm^{-2} alloy coating at cut-edge, and (b) 19 hours in contact with surface of 80% cooling output.

3.3 Cooling rate vs. surface corrosion

In a previous attempt to model the surface degradation of Galfan-type coatings, it was assumed, as is the case in cut-edge simulations, that the morphology of the dendritic phase was the dominant factor in the corrosion rate. However, the trend predicted did not correspond to that in experimentation. It is proposed however, the influence of the depressions around the eutectic cells present dictates the localized corrosion effects that ensue. The cell size has been observed to decrease with an increase in cooling rate [1], giving the greatest opportunity for the dendrites to be present at the surface for the faster cooled coating layers. Fig. 4 shows the solid model including the steel substrate at A, primary zinc and eutectic cell depressions with slices showing the electrical potentials into the electrolyte at 30 μm intervals. The effect of the surface depressions is evident, where the incidents of anodic attack do not, as was the case in Brown and Barnard [11], occur evenly over the surface but at positions along depressions. The anodic potentials still correspond to those sites where dendrites make it to the surface. Interestingly, from Fig. 4 the anodic effects present at the points indicated at B do not consistently impact the voltage field in the electrolyte at regions remote from the corroding surface (where an SVET would operate). The authors are thus reluctant to express the corrosion rate as a function of anode lifetime or dendrite removal predicted at 100 μm as in much experimental reporting.

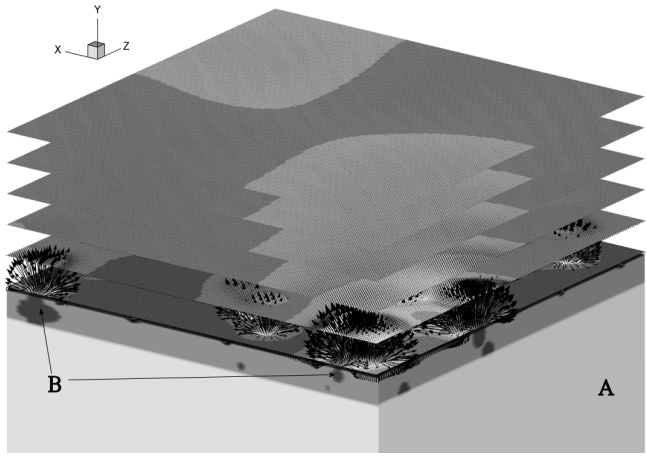

Figure 4: Planes showing anodic (light) to cathodic electrical potentials from the solid electrolyte interface to 150 μm above; current density vectors also shown.

Fig. 5 shows the predicted vertical current densities 100 μm above the solid model. It can be seen from Fig. 4 that this is a degraded representation but nevertheless a source of validation. A coupled approach to SVET experimentation and numerical prediction also considers this [12]. Fig. 5 shows a marked decrease in the frequency of anodic instances from Brown and Barnard [11] and it is apparent that the reduction in eutectic size corresponds to an increase in corrosion rate. The intensity of the anodic events is now more consistent within simulations and observation.

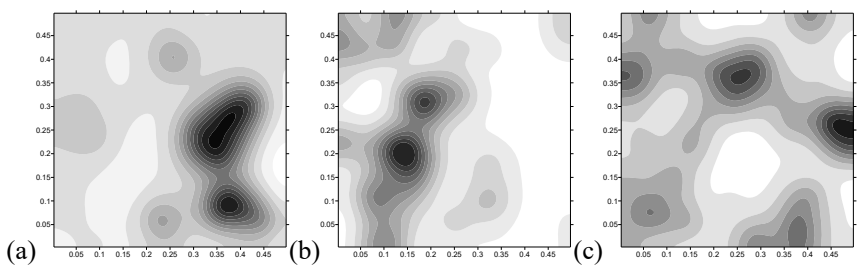

Figure 5: Vertical current density maps 100 μm above ZnAl coating after 12 hours exposure: white –3.5 $A \cdot m^{-2}$ to black +3.5 $A \cdot m^{-2}$. (a) 55%, (b) 80% and (c) 100% cooler output power (length scale mm).

In addition to the increased corrosion rate, decreasing the eutectic cell size coincides with an increase in maximum pit depth: rising from 14.6 μm to 19.2 μm over a 24-hour period – a clear indication of the relative barrier properties.

3.4 Coating weight vs. cut-edge corrosion

In simulating the cut-edge corrosion at differing coating weights, coating thickness, dendrite morphology and volume fraction of the primary phase will all have a significant influence. Fig. 6(a) shows that the material loss during the early stages of accelerated corrosion testing can be almost indistinguishable. After 2 hours simulated exposure to 5% NaCl solution, differences in the coating layers can be seen to take effect. It is the 150 gm^{-2} coating weight that exhibits the greatest acceleration in mass loss rate. As the steel substrate thickness in all cases is equivalent, the greatest anodic activity would be expected at this coating weight since the cathode to anode area is greatest in this case. This is further compounded by the increase in primary phase fraction. In Fig. 6(a), at certain exposure times, the degree of corrosion of the 255 gm^{-2} all can be seen to be equivalent to both 150 gm^{-2} and 300 gm^{-2} coating weights. This would seem to suggest that at the initial solid-electrolyte interface, the dendrite morphology plays a less significant role than volume fraction and coating thickness, but dendrite mass (smaller in lesser coating weights) becomes more significant later on exacerbating the situation in the 150 gm^{-2} coating later in the simulation. Also evident in Fig. 6(a) is the adjustment of the time step ensuring that no solid fraction greater than that present at the interface can transform in 1 time step.

Fig. 6(b) shows the total material removed from the solid model over a simulated 24-hour period. It can be seen that the greatest material loss is experienced by the 150 gm^{-2} coating, and decreases as the coating weight is increased. This is in good agreement with experimentation, although as can be seen in Fig. 6(b) the simulated mass loss is an underestimation, however the experimental findings themselves are calculated from current density maps [3].

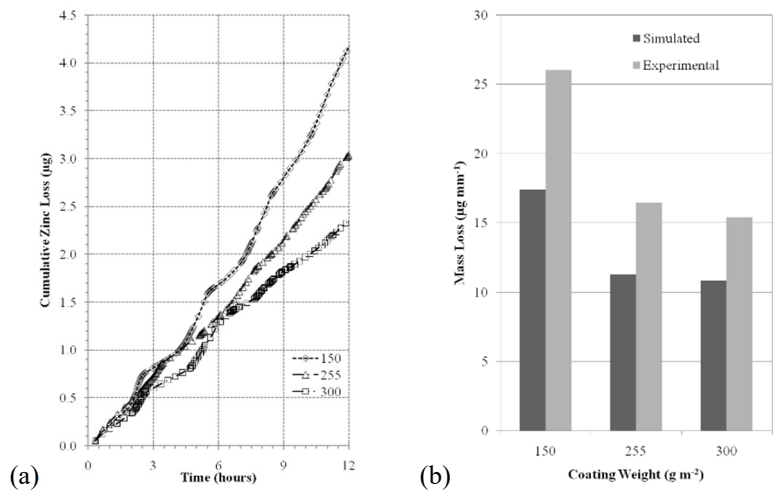

Figure 6: Material loss from the exposed steel cut-edge coated at different weights of ZnAl; (a) cumulative loss over 12 hours, and (b) mass loss during 24 hours' exposure compared with SVET testing [3].

Also in agreement is the changing trend as, unlike in cooling rate where a linear trend is observed, the decrease in mass loss as coating weight is increased is not linear and the difference between 255 gm^{-2} and 300 gm^{-2} is to a much lesser extent than is the case between 150 gm^{-2} and 255 gm^{-2}.

In terms of validating the model the most accessible data is that from SVET testing. Fig. 7 shows the vertical current density 100 μm above the initial solid-electrolyte interface after 12 hours simulated exposure. The form of the current density maps compare favourably to those reported [3]. The intensity of anodic events corresponding to the coating layer can be seen to decrease as the coating weight increases and it would be expected that heavier coating weights would experience lower delamination of applied organic coating layers. Curiously, the emergence of one coating layer offering the bulk of cathodic protection to the steel at heavier coating weights is also predicted by the model, which cannot be attributed to processing conditions since the coating layers are formed using the same parameters.

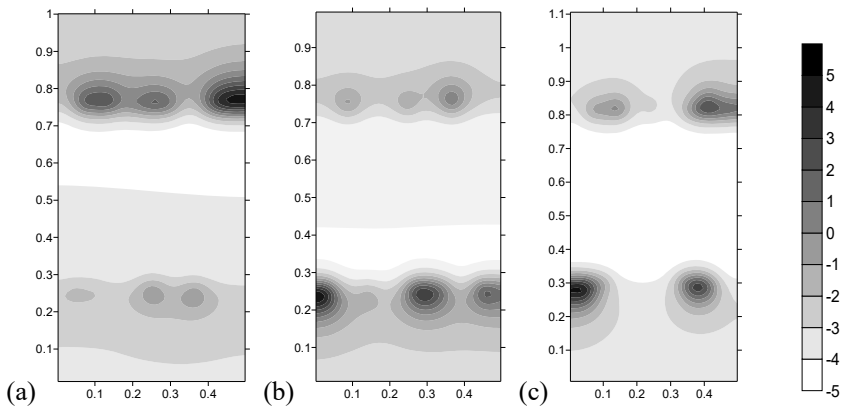

Figure 7: Vertical current density maps, J_y ($A \cdot m^{-2}$) 100 μm above ZnAl-coated steel after 12 hours exposure; (a) 150 gm^{-2}, (b) 255 gm^{-2} and (c) 300 gm^{-2} (length scale mm).

4 Conclusions

Extensions to a previously described algorithm have resulted in the capability for the prediction of corrosion at both the surface and cut-edge of steels coated with Galfan-type zinc-aluminium coatings. Using well-established electrochemical relationships and straight-forward finite difference techniques, the relationship between corrosion performance and coating weight of ZnAl coatings at an exposed cut-edge has been successfully simulated.

References

[1] Elvins, J., Spittle, J.A. & Worsley, D.A., Microstructural changes in zinc aluminium alloy galvanising as a function of processing parameters and their influence on corrosion. *Corrosion Science*, **47(11)**, pp. 2740–2759, 2005.

[2] Elvins, J., Spittle, J.A. & Worsley, D.A., The effect of low level magnesium additions on the microstructure and corrosion resistance of zinc aluminum alloy galvanized steels. *Proc. of the 7th International Conference on Zinc and Zinc Alloy Coated Steel Sheet*, Osaka, Japan: Iron and Steel Institute of Japan, pp. 653–658, 2007.

[3] Penney, D.J., Sullivan, J.H. & Worsley, D.A., Investigation into the effects of metallic coating thickness on the corrosion properties of Zn–Al alloy galvanising coatings. *Corrosion Science*, **49(3)**, pp. 1321–1339, 2007.

[4] Worsley, D.A., McMurray, H.N. & Belghazi, A., Determination of localised corrosion mechanisms using a scanning vibrating reference electrode technique. *Chemical Communications*, **24**, pp. 2369–2370, 1997.

[5] Barnard, N.C., Brown, S.G.R. & McMurray, H.N., Modelling the localized corrosion effects experienced by zinc–4.5wt.% aluminium steel coatings in 5% NaCl solution. *WIT Transactions on Engineering Sciences*, **48**, pp. 99–108, 2005.

[6] Malki, B. & Baroux, B., Computer simulation of the corrosion pit growth. *Corrosion Science*, **47(1)**, pp. 171–182, 2005.

[7] Córdoba-Torres, P., Nogueira, R.P., de Miranda, L., Brenig, L., Wallenborn, J. & Fairén, V., Cellular automaton simulation of a simple corrosion mechanism: mesoscopic heterogeneity versus macroscopic homogeneity. *Electrochimica Acta*, **46(19)**, pp. 2975–2989, 2001.

[8] Pidaparti, R.M., Fang, L. & Palakal, M.J., Computational simulation of multi-pit corrosion process in materials. *Computational Materials Science*, **41(3)**, pp. 255–265, 2008.

[9] La Rocca A. & Power H., Free mesh radial basis function collocation approach for the numerical solution of system of multi-ion electrolytes. *International Journal for Numerical Methods in Engineering*, **64(13)**, pp. 1699–1734, 2005.

[10] Souto, R.M., González-García, Y., Bastos, A.C. & Simões, A.M., Investigating corrosion processes in the micrometric range: A SVET study of the galvanic corrosion of zinc coupled with iron. *Corrosion Science*, **49(12)**, pp. 4568–4580, 2007.

[11] Brown, S.G.R. & Barnard, N.C., Micro-scale computer modelling of the relationship between metallurgical microstructure and localized corrosion effects. *WIT Transactions on Engineering Sciences*, **54**, pp. 3–12, 2007.

[12] Thébault, F., Vuillemin, B., Oltra, R., Ogle, K. & Allely C., Investigation of self-healing mechanism on galvanized steels cut edges by coupling SVET and numerical modelling. *Electrochimica Acta*, **53(16)**, pp. 5226–5234, 2008.